

## Verification and experimental validation of a numerical simulation of natural convection in a slender cylinder

José Núñez<sup>a</sup>, Miguel López-Caballero<sup>a</sup>, Eduardo Ramos<sup>a,\*</sup>, Guillermo Hernández-Cruz<sup>a</sup>,  
Minerva Vargas<sup>b</sup>, Sergio Cuevas<sup>a</sup>

<sup>a</sup> Centro de Investigación en Energía, Universidad Nacional Autónoma de México, Privada Xochicalco, 62580 Temixco, Mor., Mexico

<sup>b</sup> Instituto Tecnológico de Zacatepec, 62780 Zacatepec, Mor., Mexico

### ARTICLE INFO

#### Article history:

Received 12 July 2011

Received in revised form 5 September 2012

Accepted 13 September 2012

Available online 12 October 2012

#### Keywords:

Natural convection

Numerical verification and experimental validation

Finite volume

### ABSTRACT

Steady and time dependent natural convection of water confined in a vertical cylindrical container heated from below is studied experimentally and numerically. The container has a circular cross-section and an aspect ratio (height/diameter) of 1.25. Convective motions are analyzed for a constant Prandtl number of 6.7 and a range of Rayleigh numbers from  $3.0 \times 10^5$  to  $2.0 \times 10^6$ . These conditions include steady and time-dependent flows and in all cases, flow patterns present complex three-dimensional structures. Experimental observations were made with a composed PIV system capable of simultaneously obtaining velocity distributions in two mutually perpendicular planes. The numerical model comprises the solution of the three-dimensional time-dependent Boussinesq equations in cylindrical coordinates. Experimental observations are compared with the numerical model and a satisfactory agreement is obtained for steady flow and averaged values in unsteady flow. The general structure of the present study follows the procedure required for the verification of the numerical model and its validation with experimental observations.

© 2012 Elsevier Inc. All rights reserved.

### 1. Introduction

Natural convection in cavities has been studied from the academic point of view because of its rich dynamic behavior and also because of the challenges that it presents for proper modeling. In this line, numerical simulations of natural convection in slender cavities have been used as benchmark problems to assess the accuracy of numerical methods. In addition, this phenomenon has attracted much attention due to potential applications in the field of crystal growth where techniques like Czochralski, Bridgman and zone-melting involve natural convective motions that are determinant for the quality of the crystal. Recent monographs on the subject are Lappa (2010) and Duffar (2010).

The flow analyzed here is similar to the Rayleigh–Benard flow that describes the natural convection in a layer of fluid subject to a destabilizing temperature gradient, but with a strong influence of the lateral wall. It is well established that the convective pattern can be specified with three parameters, the aspect ratio ( $a$  = height/diameter), the Prandtl number and the Rayleigh number.

Although numerous analyses presently available in the literature have addressed various aspects of natural convection in cylindrical containers, most of them refer to features different from the

ones studied in the present investigation. For this reason, we will restrict the review to only the most closely related studies. Early investigations clarified the stability of the flow and determined the critical Rayleigh number for the onset of convection as a function of the aspect ratio of the container. The linear perturbation theory of Charlson and Sani is based on a variational formulation and uses the Rayleigh–Ritz method to solve the linearized equations that allows the calculation of the first critical Rayleigh number. They examined the cases where the convective flow is axisymmetric (Charlson and Sani, 1970) and non-axisymmetric (Charlson and Sani, 1971). Their results indicate that the stable steady state flow is non-axisymmetric (azimuthal mode  $m = 1$ ) for  $a > 0.62$  and occurs at  $Ra \approx 6590$  for a container with  $a = 1.25$  and adiabatic walls. The critical Rayleigh numbers for the onset of convection were also calculated with linear Galerkin method by Buell and Catton (1983) finding critical Rayleigh numbers up to 20% smaller than those obtained by Charlson and Sani for the non-axisymmetric modes.

Experimental investigations of the convective instabilities in closed vertical cylinders have been made using arrangements of thermal sensors to infer global dynamic features of the flow (see for instance Olson and Rosenberger, 1979). Although relevant results on the critical Rayleigh numbers have been found with this technique that confirm the theoretical predictions for  $a = 3$ , details of the motion were not resolved.

\* Corresponding author.

E-mail address: [erm@cie.unam.mx](mailto:erm@cie.unam.mx) (E. Ramos).

## Nomenclature

### Latin symbols

$a$	aspect ratio of the cylinder ( $h/D$ )
$D$	diameter of the cylinder
$g$	terrestrial gravity acceleration
$h$	height of the cylinder
$p$	pressure
$Pr$	Prandtl number ( $\nu/\alpha$ )
$r$	radial coordinate
$R_\psi$	rotation operator around an azimuthal angle $\psi$
$Ra$	Rayleigh number ( $g\beta\Delta T h^3/\nu\alpha$ )
$T$	temperature
$T_H$	temperature of the lower wall of the container
$T_C$	temperature of the upper wall of the container
$u_c$	free fall velocity ( $\sqrt{g\beta\Delta T h}$ )
$u_r$	velocity component in the radial direction
$u_\theta$	velocity component in the azimuthal direction

$u_z$	velocity component in the axial direction
$z$	axial coordinate

### Greek symbols

$\alpha$	thermal diffusivity
$\beta$	volumetric expansion coefficient
$\Delta T$	Temperature difference between hot and cold walls ( $T_H - T_C$ )
$\theta$	azimuthal coordinate
$\nu$	kinematic viscosity
$\rho$	density
$\Omega_h$	$\pi/2$ rotation around the horizontal line passing through the center of the cylinder
$\Omega_v$	$\pi/2$ rotation around the vertical line passing through the center of the cylinder

The theoretical and experimental investigation of Müller et al. (1984) on the convective patterns in cylindrical container is closely related to the present study and deserves a somewhat detailed description. They made qualitative observations of motion inside water filled cylinders with aspect ratios ranging from 0.5 to 5 using the light cut technique which yields observations of the flow patterns in planes. A stability diagram ( $Ra$  vs  $a$ ) indicating the regions with no flow, steady and time-dependent flow is presented. They report that the steady, two dimensional flow pattern observed for  $a = 1$  and  $Ra = 17,500$  is different depending on the orientation of the vertical plane observed. For one plane (of unspecified orientation), a single, non-axisymmetric cell is found, while the pattern in the perpendicular plane is composed of four rolls. The observations were interpreted with a theoretical model obtained by numerically solving the conservation equations. They described the non-axisymmetric flow patterns obtained for  $a = 1$  in terms of the vertical velocity at horizontal planes and explained that the flow is rather complicated with a three dimensional structure.

Neumann (1990), obtained a numerical solution based on the finite differences discretization of the conservation equations with boundary conditions corresponding to natural convective flow in cylinders heated from below. The solution was found using cylindrical coordinates and a mesh of 20 points in the  $r$ ,  $\theta$ , and  $z$  directions. The aspect ratio of the cylinders considered are 0.5 and 1 which are, according to the linear theories, below and above the critical aspect ratio for the transition from axisymmetric to non-axisymmetric flow patterns. In the second case, he obtains a steady state, non-axisymmetric flow composed of a single convective cell for  $Ra = 5 \times 10^4$  and  $Pr = 6.7$  with fluid ascending on one side of the cavity and descending on the opposite with the orientation of the roll given by the initial temperature distribution. His results are in qualitative agreement with experimental results of Müller et al. (1984).

A finite difference method was also used by Crespo del Arco et al. (1988) to simulate natural convection in cylinders. They described the features of steady and time dependent non-axisymmetric convective patterns with  $a = 2$  and Prandtl number 0.002.

The general structure of the present study follows the procedure required for verification and validation of a model as defined by Schlesinger (1979). Following the criteria established by Oberkampf and Trucano (2002), we emphasize that the purpose of the numerical model is to produce velocity fields that can be compared with the experimental observations. The domain of application for the model is the range of Rayleigh numbers that are observed in the experiment and the level of agreement expected is the coincidence within the experimental error.

## 2. Experimental setup

The experimental device is composed of a 2 mm wall thickness soda lime glass tube with circular cross-section. The diameter and height of the tube are 16 mm and 20 mm, respectively. Two heat exchangers constitute the top and bottom walls to conform a container; the lower heat exchanger maintains a constant high temperature  $T_H$  and is a two piece rectangular cross-section case that forms a cavity where controlled temperature water flows. In the upper side of this heat exchanger, a 1 mm deep circular O ring bed accommodates the ring that seals the region where the heat exchanger and the glass tube meet. The upper heat exchanger maintains a constant cold temperature  $T_C$  and is also a cavity where cold temperature controlled water flows and is made of a transparent piece to allow optical access from the upper vertical direction. The circular cross-section tube is encased inside a shroud made of a rectangular cross-section glass tube that is also fixed by the upper and lower heat exchangers; water fills the volume between the two glass tubes to facilitate lateral optical access. This cover also thermally insulates the inner cylinder from the temperature fluctuations in the environment. Hot and cold water for the heat exchangers are supplied by thermal baths and pumps. Typical flow rates in the heat exchangers are  $3 \times 10^{-3}$  l/s; the thermal baths keep constant the water temperatures in the heat exchangers.

The working fluid was distilled water, and 10  $\mu$ m diameter, neutrally buoyant, hollow glass spheres were used as tracers. Special care was put to guarantee that the tracers were neutrally buoyant to prevent floating or sedimentation that might affect the measurements. Velocity fields of the convective flows occurring inside the inner container were recorded simultaneously in vertical and horizontal planes using two independent and mutually perpendicular PIV systems. The light source for the vertical PIV is a 300 mW, solid state, 532 nm wavelength laser (B&WTEK, model BWT-50PIG). An optical fiber conducts the light to a system equipped with a Powell lens that forms a light plane with uniform intensity (OZ Optics model FOLM-23-400/700-S-3.5AC-30). The emerging light plane has a thickness of 1 mm and a spread angle of 30°. The images of the tracer particles were captured with a Kodak MegaPlus ES 1.0 CCD camera with a spatial resolution of 648H  $\times$  575 V and a maximum frame rate of 30 fps. A narrow band filter centered in 534 nm was used to prevent stray light and light from the horizontal PIV from entering into the camera.

The light source of the horizontal PIV system is a helium–neon gas, 50 mW laser tube that emits at 632.8 nm (Melles Griot model

05-LHP-927) which is coupled with an optical arrangement to generate a light plane, identical to that used in the vertical PIV. In this system, a narrow band filter centered in 632 nm was used to discriminate unwanted light. The camera of this system was a Basler (A302b) with a spatial resolution of 782H × 582V operating at 30 fps. We have used two images as the pair required by the PIV analysis and therefore, the time interval between two consecutive images (1/30 s) is used as the time increment for the velocity calculation. In the two cameras, the central plane was focused and the adjacent planes were slightly out of focus (see Fig. 1). Information from the two perpendicular planes was simultaneously obtained with a couple of frame grabbers (Labview frame grabber PCI1428 and Labview frame grabber PCI1424) mounted on the same mother board and internally synchronized. The holder of each light plane generating optics was installed on movable mounts that displace independently the horizontal and vertical light planes in the vertical and horizontal directions, respectively. Therefore, with these devices, horizontal and vertical planes inside the cavity can be illuminated at any desired height or depth, allowing the exploration of two mutually perpendicular 2D velocity fields inside the volume occupied by the working fluid. The motion of the displacement systems is driven by stepper motors.

The displacement of the light planes is automatically governed by the parallel port of a PC, programmed with a Labview software. As described before, we observed steady and time-dependent flows. For steady flows, we obtained data in the three vertical planes and three horizontal planes whose positions are shown in Fig. 1. The velocity fields reported in each position of the light planes, was obtained by averaging 15 pairs of images. The time dependent flows were observed with the recording planes fixed in their central positions (**V** and **H**) in Fig. 1. The temperature inside the cavity was monitored with two type “T” thermocouples located one millimeter away from the upper and lower horizontal walls, respectively, and in diametrically opposed positions. The temperatures of the heat exchangers were also monitored with thermocouples and their variations were less than  $\pm 0.3$  K. All temperature data was registered with a SCXI-1100 multiplexer (32 channels) coupled to a NI board (PCIMIO16E1).

We performed six experimental runs with the parameters shown in Table 1. Experiments 1 and 2 were made to test the repeatability of our observations. Although there is a difference of 4% in the temperature gradients (and Rayleigh numbers) we observed the same velocity magnitudes within the experimental error in sample checks. This approximate coincidence indicated the consistency of our observations. In the first three runs, the flow

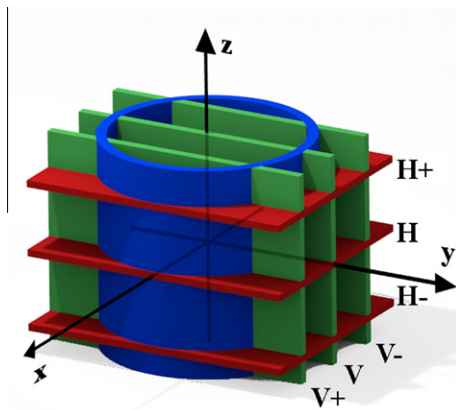


**Fig. 1.** Positions of the horizontal (**H**) and vertical (**V**) planes where experimental observations were made. Planes **V** ± are located at  $\pm 4$  mm from the central vertical plane, while planes **H** ± are located at  $\pm 5$  mm from the central horizontal plane. For future reference (Section 4.1.1), a two dimensional Cartesian coordinate system is defined on plane **V**, with the origin of coordinates at its center.

**Table 1**

Temperature difference  $\Delta T$  and Rayleigh number  $Ra$  for experimental runs.

	$\Delta T$ (°C)	$Ra$
1	2.4	$3.07 \times 10^5$
2	2.5	$3.20 \times 10^5$
3	4.0	$5.12 \times 10^5$
4	11.4	$1.46 \times 10^6$
5	12.0	$1.53 \times 10^6$
6	15.6	$2.00 \times 10^6$

was steady, while in runs 4–6 we observed a time-dependent motion.

### 3. Numerical analysis

The natural convective motion inside the cylindrical container under the conditions of interest can be described by numerically solving the mass, momentum and energy conservation equations. Given that the maximum temperature differences are small, the Boussinesq approximation is used. In the frame of this approximation, the kinematic viscosity  $\nu$ , the thermal diffusivity  $\alpha$ , and the volume expansion coefficient  $\beta$ , are constant. The density  $\rho$  is also considered constant except for the body force term in the momentum conservation equation in the axial direction, where it is a linear function of temperature. The cylindrical sidewall is chosen to be adiabatic, i.e. the temperature gradient normal to the wall is set equal to zero. At all container walls the no-slip velocity boundary condition is prescribed.

The set of conservation equations have been solved in its dimensionless form. The scaling we have used was the most convenient for the numerical solution and includes the following characteristic quantities: the axial and radial coordinates are scaled with the height ( $h$ ) of the cylinder. The characteristic velocity ( $u_c$ ) is the free fall velocity, namely  $u_c = \sqrt{g\beta\Delta Th}$ . The time scale is defined using the characteristic time  $h/u_c$  and the non-dimensional temperature is defined as  $(T - T_c)/(T_H - T_c)$ .

In dimensionless form, the governing equations written in cylindrical coordinates ( $r, \theta, z$ ) are:

$$\frac{1}{r} \frac{\partial}{\partial r}(ru_r) + \frac{1}{r} \frac{\partial u_\theta}{\partial \theta} + \frac{\partial u_z}{\partial z} = 0, \quad (1)$$

$$\frac{\partial u_r}{\partial t} + (\vec{u} \cdot \nabla)u_r - \frac{u_\theta^2}{r} = -\frac{\partial p}{\partial r} + \left(\frac{Pr}{Ra}\right)^{\frac{1}{2}} \left(\nabla^2 u_r - \frac{u_r}{r^2} - \frac{2}{r^2} \frac{\partial u_\theta}{\partial \theta}\right), \quad (2)$$

$$\frac{\partial u_\theta}{\partial t} + (\vec{u} \cdot \nabla)u_\theta + \frac{u_\theta u_r}{r} = -\frac{1}{r} \frac{\partial p}{\partial \theta} + \left(\frac{Pr}{Ra}\right)^{\frac{1}{2}} \left(\nabla^2 u_\theta - \frac{u_\theta}{r^2} + \frac{2}{r^2} \frac{\partial u_r}{\partial \theta}\right), \quad (3)$$

$$\frac{\partial u_z}{\partial t} + (\vec{u} \cdot \nabla)u_z = -\frac{\partial p}{\partial z} + \left(\frac{Pr}{Ra}\right)^{\frac{1}{2}} \nabla^2 u_z + T, \quad (4)$$

$$\frac{\partial T}{\partial t} + (\vec{u} \cdot \nabla)T = \left(\frac{1}{RaPr}\right)^{\frac{1}{2}} \nabla^2 T, \quad (5)$$

where  $\vec{u} = (u_r, u_\theta, u_z)$  is the velocity,  $p$  is the pressure and  $T$  is the temperature. The differential operators are

$$\vec{u} \cdot \nabla = u_r \frac{\partial}{\partial r} + \frac{u_\theta}{r} \frac{\partial}{\partial \theta} + u_z \frac{\partial}{\partial z}$$

and

$$\nabla^2 = \frac{1}{r} \frac{\partial}{\partial r} \left( r \frac{\partial}{\partial r} \right) + \frac{1}{r^2} \frac{\partial^2}{\partial \theta^2} + \frac{\partial^2}{\partial z^2}.$$

The flow is characterized by two dimensionless parameters, the Rayleigh and Prandtl numbers, defined by

$$Ra = \frac{g\beta\Delta Th^3}{\nu\alpha} \quad \text{and} \quad Pr = \frac{\nu}{\alpha}. \quad (6)$$

**Table 2**

Mesh refinement test for numerical accuracy of the steady flow at  $Ra = 5.12 \times 10^5$  and  $Pr = 6.7$ .

Mesh	$u_\theta^{\max}$	$u_r^{\max}$	$u_z^{\max}$
$20 \times 20 \times 20$	$8.0424488E-02$	$7.8527927E-02$	$0.1240261$
$30 \times 30 \times 30$	$7.9905130E-02$	$7.8891858E-02$	$0.1216930$
$40 \times 40 \times 40$	$7.9648100E-02$	$7.9282701E-02$	$0.1215185$

The boundary conditions corresponding to the physical situation of interest are:

$$T = 0 \quad \text{at} \quad z = -\frac{1}{2}, \quad T = 1 \quad \text{at} \quad z = \frac{1}{2}, \quad (7)$$

$$\frac{\partial T}{\partial r} = 0 \quad \text{at} \quad r = 1/(2a), \quad (8)$$

and

$$\vec{u} = 0 \quad \text{at all boundaries.} \quad (9)$$

The initial conditions for the time integrations are zero velocity in the whole volume. The initial temperature and pressure distributions along the axial direction are assumed to be linear and quadratic, respectively.

The governing equations and boundary conditions are invariant under arbitrary rotations about the axis of the cylinder. If  $R_\psi$  is a rotation of angle  $\psi$  around the  $z$ -axis, its action is

$$R_\psi(u, v, w, T, p)(r, \theta, z) = (u, v, w, T, p)(r, \theta + \psi, z). \quad (10)$$

This property indicates that if a solution is obtained, the same velocity, pressure and temperature fields with a different orientation with respect to the vertical axis, constitute also a solution. These rotations generate the symmetry group  $O(2)$ .

The conservation equations were discretized using the finite volume method and then solved numerically. The cylindrical volume is divided in small cells having edge lengths  $\Delta r$ ,  $r\Delta\theta$  and  $\Delta z$ . The derivatives in time and space were respectively approximated with first order forward differences and second order central differences. Following Neumann (1990), a staggered mesh is used with the velocity components located at the cell faces and scalar fields defined at the center of the cells. The SIMPLEC algorithm described by Patankar (1980) and VanDoormal and Raithby (1984) was used for pressure decoupling. This algorithm is iterative and stops with a small velocity divergence criterion,  $\epsilon = 10^{-5}$ . A mesh refinement calculation was done to verify the accuracy of the

numerical solution. In Table 2 we show results for the maxima of the three components of the velocity as functions of the mesh fineness. For further comments on the verification of the solution see Section 5.

Calculations are performed in cylindrical coordinates but for the comparison with the experimental observations the solution is interpolated to Cartesian coordinates to compare experimental observation and simulations in the corresponding planes.

#### 4. Results

The theoretical and experimental results presented in this section correspond to the interval  $3.0 \times 10^5 < Ra < 2.0 \times 10^6$  and in all cases the Prandtl number is 6.7. The conditions chosen for the analysis were determined by limitations in the experimental equipment and also to comply with the restrictions imposed by the Boussinesq approximation. For the smaller Rayleigh numbers considered, the flow was found to be steady, in contrast to the time dependent flow observed for the larger Rayleigh numbers. The experimentally determined critical Rayleigh number where the transition occurs is in the interval  $5.12 \times 10^5 < Ra_c < 1.46 \times 10^6$ , while the numerical calculations indicate that the transition occurs at  $Ra_c \sim 1.3 \times 10^6$ . These results agree with the (interpolated) values reported by Müller et al. (1984) for the aspect ratio of the cavity studied here. In the following subsection we describe the dynamics of the flow with  $Ra = 5.12 \times 10^5$ , and in Section 4.2, the time-averaged velocity fields for  $Ra = 1.53 \times 10^6$  are presented. The estimation of the experimental uncertainties was made according to the following procedure. As discussed in Section 2, in steady state, 15 pairs of images were captured and averaged for every experimental observation reported. Histograms of the velocity in each individual observation at every point in the velocity field allow us to calculate a standard deviation of an adjusted normal distribution. Considering the standard deviation as the uncertainty at every point of the interrogation grid, it is possible to build an uncertainty map. In the graphs where velocity is given as a function of position, the uncertainty in position is due to instrumental precision.

##### 4.1. Steady flow

For clarity in the presentation, we start by describing the structure of the flow using information from the numerical solution. Once we have identified the dominant features of the flow

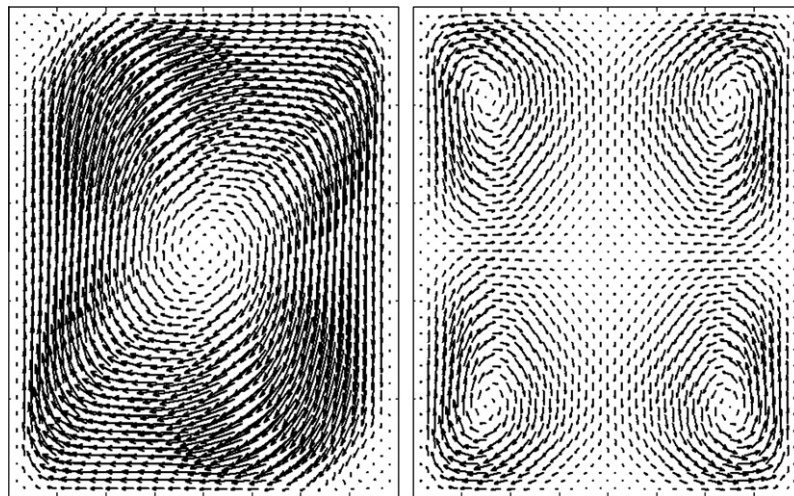


**Fig. 2.** Velocity fields in two mutually perpendicular vertical planes containing the cylinder axis. Left and right panels show respectively planes AA' and BB' of Fig. 3.



patterns, we proceed to compare with the experimental velocity fields. The velocity fields obtained with the numerical integration for  $Ra = 5.12 \times 10^5$ , which corresponds to steady flow, for two mutually perpendicular vertical planes, are shown in Fig. 2. The planes on the left and right panels of this figure are labeled AA' and BB' respectively. The left panel of Fig. 2 shows that the dominant flow pattern in plane AA' is a single convective cell rotating clockwise with its center defined by the point of vanishing velocity located near the geometrical center of the plane. Fluid ascends on one side of the plane and descends on the opposite with small vortical structures present in the left upper corner and right lower corner. The flow pattern is symmetric under the composition of two rotations  $\Omega_h \circ \Omega_v$ . The first rotation ( $\Omega_v$ ) is around a vertical axis passing through the center of the cavity and the second rotation  $\Omega_h$  is taken around the central horizontal axis. An examination of the magnitude of the velocity in the whole volume indicates that the point with maximum velocity is located in this plane. The velocity field in the right panel of the same figure indicates that the convective pattern in plane BB' is composed of four rotating structures one in each quadrant of the rectangle. The velocity distribution displays specular symmetry with respect to the vertical and horizontal lines passing through the center of the rectangular plane, i.e. the velocity distributions is symmetric with respect to  $\Omega_h$  and  $\Omega_v$ .

The remarks leading to Eq. (10) indicate that there is no preferred orientation implicit in the conservation equations and boundary conditions. However, as indicated in the left panel of Fig. 2, the solution is clearly non-axisymmetric and solutions with the same convective pattern, but different azimuthal orientations exist. The calculation procedure used in the numerical integration defines a specific orientation of the convective pattern, and for this reason we have no control on the resulting orientation of the calculated flow. It was found that the symmetries described in the flow shown in the right panel of Fig. 2 occurs only in this particular plane. Hence, this plane can be used as a reference for the definition of the orientation of the convective cell. In all other planes containing the axis of the cylinder, it was observed that the flow does not feature these symmetries but are smooth transitions from one of the two patterns in Fig. 2 to the other.

In order to give a global idea of the flow inside the cavity, we use the concept of *vortex core* as a visualization tool, calculated according to the definition of Jeong and Hussain (1995) and shown

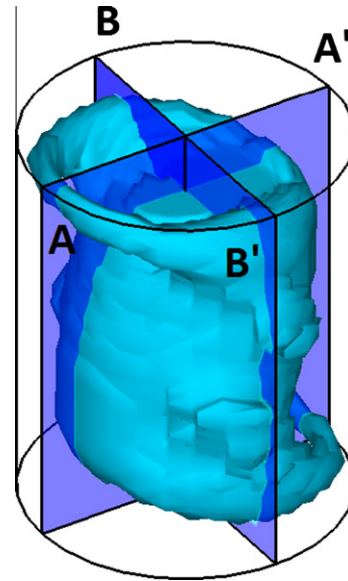


Fig. 3. Vortex core for  $Ra = 5.12 \times 10^5$ .

in Fig. 3. The volume contained in the vortex core indicates the region where local rotational motion dominates over strain deformation. The outline of the container and the position of planes AA' and BB' are also shown in Fig. 3. As expected, the vortex core is not axisymmetric but displays clearly the symmetries discussed in the context of Fig. 2.

It is found that the temperature distributions are deformed by the convective motion, but in a large part of the volume, the temperature has approximately the same value. In some experimental studies reported in the literature, the flow has been characterized by a local recording of the temperature. But given that the temperature gradients are small, the correct positioning of the temperature sensors is critical for this characterization strategy and therefore not recommended.

#### 4.1.1. Comparison with experimental data

As explained in previous sections, a cylindrical coordinate system was used for the numerical calculations, while the information from the experimental system was acquired by moving the light

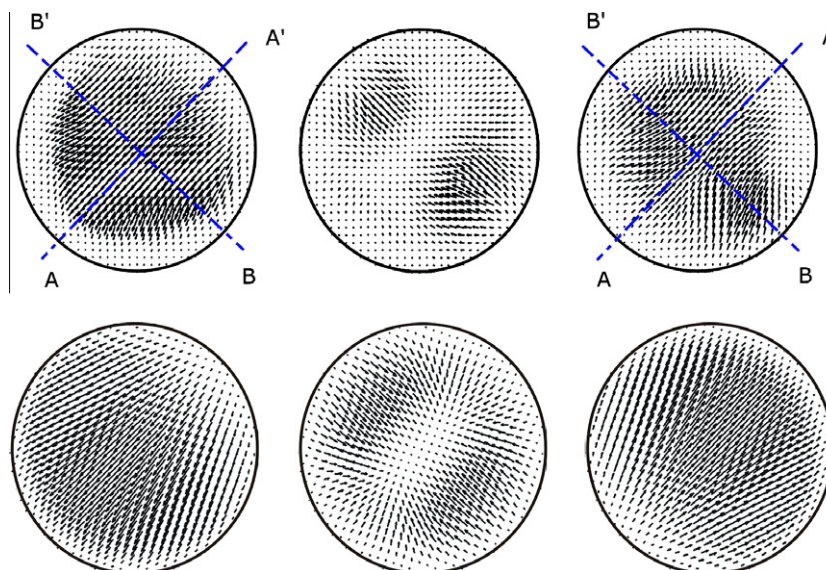
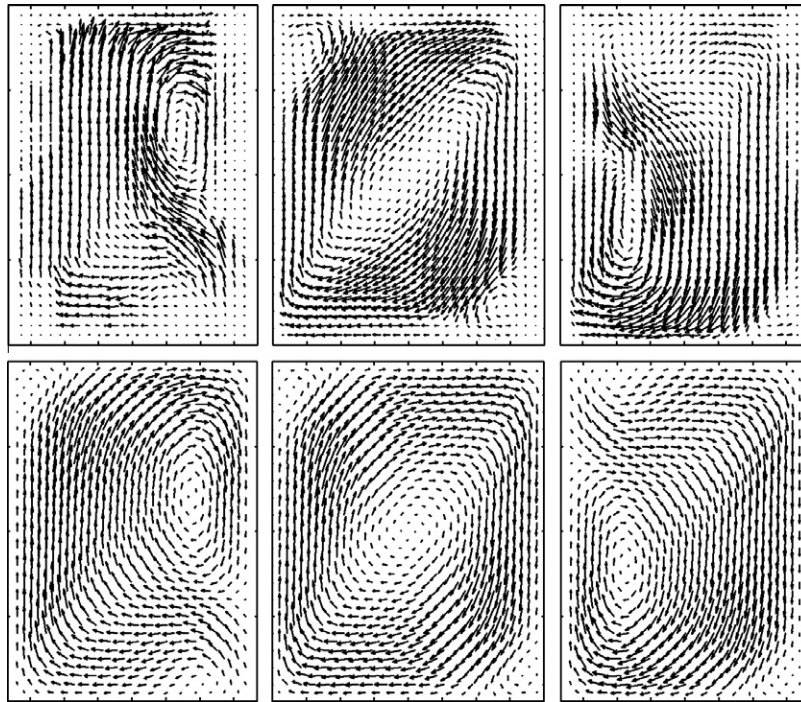


Fig. 4. Upper row, experimental horizontal projection of the velocity field; lower row, calculated horizontal projection of the velocity field. The first, second and third columns correspond, respectively, to planes H<sup>-</sup>, H and H<sup>+</sup> of Fig. 1. The positions of planes AA' and BB' are illustrated for upper (H<sup>+</sup>) and lower (H<sup>-</sup>) observed velocity fields.



**Fig. 5.** Upper row, experimental vertical projection of the velocity field; lower row, calculated vertical projection of the velocity field. The first, second and third columns correspond respectively to planes  $V^-$ ,  $V$  and  $V^+$  of Fig. 1.

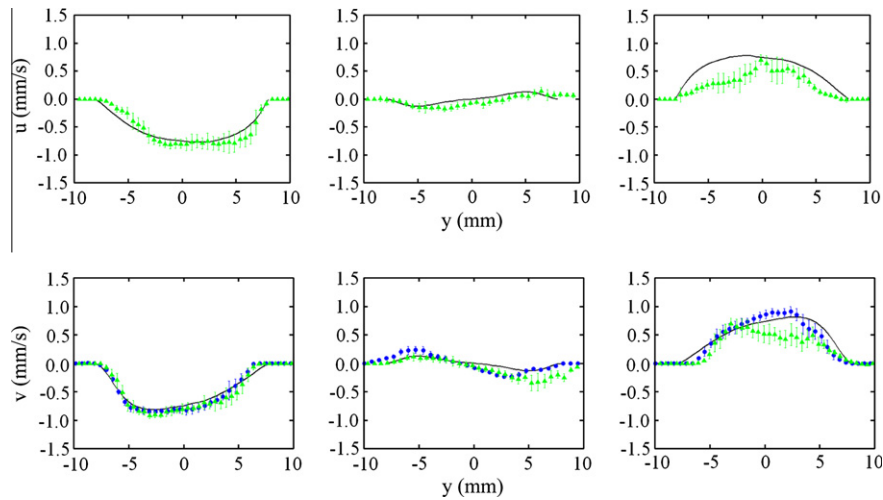
planes in Cartesian directions; see Fig. 1. Hence, in order to compare the theoretical and experimental results, interpolations were required. Given that the density of data in the calculations is far larger than that of the experimental observations, we chose to interpolate the numerical calculations to find the velocities in the points where the experimental data were observed. We attempt to compare the projection of the velocity field on a vertical plane that contains the axis of the cylinder (plane  $V$  in Fig. 1), but since the orientation of the experimentally observed plane is not known a priori, it is required to search for the best fit of the calculated velocity fields with different orientations. Even though all orientations can be calculated, we find that this is not a straightforward task since differences between calculated velocity fields and the experimentally observed velocity field are similar for a relatively wide range of orientations and it is difficult to single out the optimum orientation. However, using information from the velocity fields in the horizontal planes, the orientation is relatively simple to find. Fig. 4 shows the experimental (upper row) and calculated (lower row) projection of the velocity field on the three horizontal planes,  $H^+$ ,  $H$  and  $H^-$  of Fig. 1. As can be clearly seen, the velocity fields display the same qualitative features. The first and last velocity fields show that the flow is mostly one directional and in opposite sense from each other; the central field displays a sink at the center of the circular region. The orientation of the plane  $AA'$  is parallel to the direction of the flow of the velocity distribution near the central region in  $H^-$  (or  $H^+$ ). The plane  $BB'$  is orthogonal to  $AA'$ . Position of these planes are also displayed in Fig. 4.

Fig. 5 shows the velocity field projections in vertical planes  $V^-$ ,  $V$  and  $V^+$  of Fig. 1. As can be appreciated, all major features of the flow are correctly captured by the numerical solution, in particular, the displacements of the center of the dominant vortex as the planes examined are moved toward ( $V^+$ ) or away ( $V^-$ ) from the observer. Another interesting feature clearly displayed in both velocity fields at position ( $V$ ) are the two small counter-rotating cells in the upper left and lower right corners.

In order to make a quantitative comparison between numerical calculations and experimental observations, we plot the components of the velocity field as functions of the Cartesian coordinate  $y$ , defined as the horizontal coordinate. The origin of coordinates is located at the center of the central  $V$  plane. The velocity distributions are taken at  $z = -5.0$  mm,  $z = 0$  and  $z = 5.0$  mm. In the upper and lower rows of Fig. 6, the velocity components  $u$  and  $v$  are plotted as a function of  $y$ . The dots are experimental observations and the continuous lines are numerical calculations; the green<sup>1</sup> and blue dots were obtained with the horizontal and vertical PIV systems, respectively. The experimental information on the velocity components was obtained beyond the limits of the cell walls and correctly gives zero values. The numerical calculation is made strictly in the region occupied by the fluid and the curves were drawn just between these limits. The method to calculate the experimental uncertainty is described in the first paragraph of this section.

As can be appreciated in Fig. 6, experimental observations coincide with the numerically calculated velocity profiles in most cases. It is interesting to note that the largest discrepancies between the numerical calculations and the observations are found for the green dots (horizontal PIV system) and  $z = 5.0$  mm where limitations in the experimental equipment result in poor quality of the PIV images. Also, for the same reason, in this location the uncertainty bars are the largest. Fig. 7, shows the vertical velocity  $w$  profiles at the plane  $V$  and  $z = -5.0$  mm, 0 and 5.0 mm as functions of  $y$ . At the center of the cavity, where the velocity is larger, the observed and calculated profiles coincide quantitatively. Above and below these positions, although there is a qualitative coincidence, the calculated profiles underestimate the observed velocities in some intervals.

<sup>1</sup> For interpretation of color in Fig. 6, the reader is referred to the web version of this article.



**Fig. 6.** Upper row:  $x$ -velocity component  $u$  as a function of  $y$ . Left,  $z = -5.0$  mm, center  $z = 0$  right  $z = 5.0$  mm. The continuous lines are numerical calculations and the dots are experimental observations. Green and blue dots are data obtained with the horizontal and vertical PIV systems respectively. Lower row:  $y$ -velocity component  $v$  as a function of  $y$  for the same vertical locations as in the upper line.

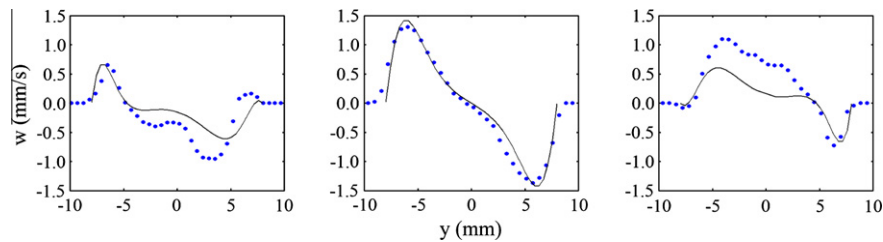


**Fig. 7.** Numerical and experimental  $w$  velocity component in the central vertical plane as a function of  $y$  at  $z = -5.0$  mm (left),  $z = 0$  (center)  $z = 5.0$  mm (right).

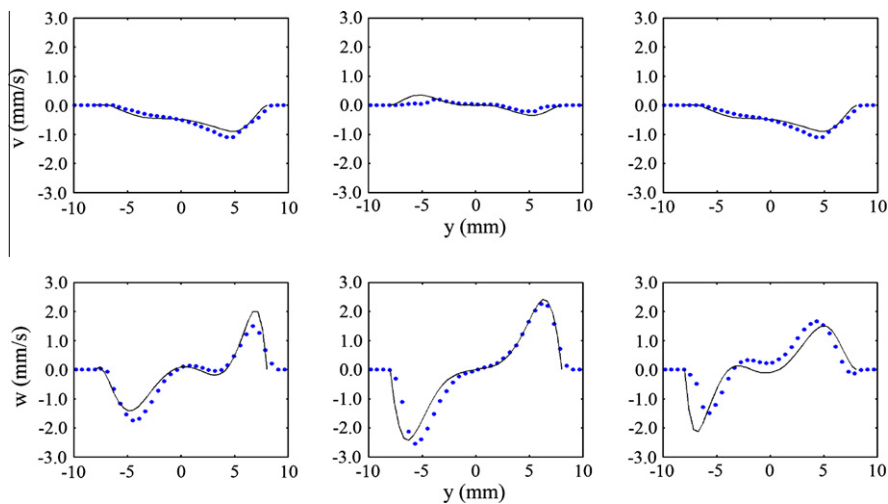


**Fig. 8.** Upper row, average  $y$ -velocity  $v$  as a function of the horizontal coordinate  $y$ . Lower row, average  $z$ -velocity  $w$  as a function of the horizontal coordinate  $y$ . Left column,  $z = 5.0$  mm, center column,  $z = 0$ , right column  $z = -5.0$  mm.  $Ra = 1.53 \times 10^6$ .

#### 4.2. Time dependent flow

The results presented in this section correspond to the unsteady flow occurring at  $Ra = 1.53 \times 10^6$ . Given the time-dependent nature of this flow, it was not possible to explore more than one vertical plane with the present experimental equipment. Also, no attempt was made to resolve the dynamics of the flow since the time resolution of the cameras was not fast enough to record the flow evolution. In addition, memory limitations in our equipment did not allow us to capture more than 300 subsequent images.

We obtained time average velocity fields using 1760 vector fields which correspond to 540 s long observations in the center vertical plane **V**. The numerical calculations indicate that the flow is periodic with an approximate characteristic time of 9 s and although the detailed time evolution of the flow does not coincide with experimental records, we are able to compare theoretical and experimental averaged velocity fields.

The dominant averaged convective structure is a single convective cell, similar to that observed in the steady state flow with two small counter rotating cells at the upper left and lower right



corners. The corresponding numerical simulation displays the same features.

Quantitative comparisons of the velocity profiles have been made using the same geometrical nomenclature and definitions of Section 4.1. Fig. 8 shows experimental and numerical results of  $v$  and  $w$  at  $z = -5.0$  mm,  $z = 0$  and  $z = 5.0$  mm.

As observed in Fig. 8, the qualitative behavior calculated with the numerical model agrees with the corresponding experimental data in all cases. Also, the quantitative differences are small in most cases, particularly for the vertical component of the velocity where the signal to noise ratio is largest.

## 5. Discussion and conclusions

Experimental and numerical investigations of steady and time-dependent natural convection in a slender cylindrical cavity filled with water and heated from below are reported. Steady and time-dependent flows were considered. We have followed the verification and validation methodology<sup>2</sup> to test adequacy of the physical model and numerical solution.

As a further verification of the numerical calculations, we solved the governing equations with a spectral method using Fourier–Galerkin for the azimuthal coordinate and Chebyshev polynomials for the radial and axial coordinates; we used the projection method for pressure decoupling described by Mercader et al. (2010). Both methodologies gave equivalent results for the steady convective flow in the cylinder. Given that the finite volume method is a simpler methodology, we used it for obtaining the results presented in this report. Since the numerical solution is independent of the mesh and two different discretization methods give coincident results, the numerical solution was considered to be verified.

Although studies of flows similar to the one studied here are available in the literature, there have been very few attempts at detailed comparison between experimental observations and calculations from numerical simulations for natural convection flows. The present study contains such a comparison for a particular aspect ratio and range of Rayleigh numbers. In the context of numerical model credibility, this procedure constitutes the validation. It is interesting to note that a particular difficulty of the analysis of the flow explored here is the fact that the azimuthal orientation of the experimentally observed non-axisymmetric convective cell is not known. We solved this problem by simultaneously recording

the velocity in horizontal and vertical planes. We conclude that the qualitative features of the observed flow are correctly modeled by the numerical solution and that in many specific comparisons, a quantitative agreement has been found. In turn, the numerical solution gives valuable information on flow features not directly observed.

## Acknowledgments

Guillermo Ramírez and Heberto Pérez made the technical drawings and Dr. Fernando Sierra made an early version of the convective cell. J. Núñez and M. López received postgraduate grants from CONACyT (Mexico). This work was partially financed by CONACyT (Mexico) through project No. 131399 “Flujos magneto-hidrodinámicos en campos magnéticos inhomogéneos”.

## References

- Aeschliman, D.P., Oberkampf, W.L., Blottner, F.G., 1995. A proposed methodology for computational fluid dynamics code verification, calibration, and validation. *International Congress on Instrumentation in Aerospace Simulation Facilities* 16, 255–260.
- Buell, J.C., Catton, I., 1983. The effect of wall conduction on the stability of a fluid in a right circular cylinder heated from below. *J. Heat Trans.* 105, 255–260.
- Charlson, G.S., Sani, R.L., 1970. Thermoconvective instability in a bounded cylindrical fluid layer. *Int. J. Heat Mass Trans.* 13, 1479–1495.
- Charlson, G.S., Sani, R.L., 1971. On the thermoconvective instability in a bounded cylindrical fluid layer. *Int. J. Heat Mass Trans.* 14, 2157–2160.
- Crespo del Arco, E., Bontoux, P., Sani, R.L., Hardin, G., Extrémet, G.P., 1988. Steady and oscillatory convection in vertical cylinders heated from below. *Numerical simulation of asymmetric flow regimes. Adv. Space Res.* 8 (12), 281–292.
- Duffar, T., 2010. *Crystal Growth Processes Based on Capillarity*. Wiley.
- Jeong, J., Hussain, F., 1995. On the identification of a vortex. *J. Fluid Mech.* 285, 69–94.
- Lappa, M., 2010. *Thermal Convection, Patterns, Evolution and Stability*. Wiley.
- Mercader, I., Batiste, O., Alonso, A., 2010. An efficient spectral code for incompressible flows in cylindrical geometries. *Comput. Fluids* 39 (2), 215–224.
- Müller, G., Neumann, G., Weber, W., 1984. Natural convection in vertical Bridgman configurations. *J. Cryst. Growth* 70, 78–93.
- Neumann, G., 1990. Three-dimensional numerical simulation of buoyancy-driven convection in vertical cylinders heated from below. *J. Fluid Mech.* 214, 559–578.
- Oberkampf, W.L., Trucano, T.G., 2002. Verification and validation in computational fluid dynamics. *Prog. Aerosp. Sci.* 38, 209–272.
- Olson, J.M., Rosenberger, F., 1979. Convective instabilities in a closed vertical cylinder heated from below. Part 1. Monocomponent gases. *J. Fluid Mech.* 92, 609–629.
- Patankar, S.V., 1980. *Numerical Heat Transfer and Fluid Flow*. McGraw Hill.
- Schlesinger, S., 1979. Terminology for model credibility. *Simulation* 32, 103–104.
- VanDoormal, J.R., Raithby, G.D., 1984. Enhancements of the simple method for predicting incompressible fluid flows. *Numer. Heat Trans.* 7, 147–163.

<sup>2</sup> According to Aeschliman et al. (1995) verification is guaranteeing that the results obtained with an approximate numerical integration are independent of the method of integration used. *Validation* is the comparison of the results of the numerical model and the experimental observations to determine the range of parameters for which the comparison is satisfactory.